Received: 6 February 2021 | Accepted: 5 March 2021

DOI: 10.1002/htj.22132

RESEARCH ARTICLE

HEAT TRANSFER WILEY

Numerical and sensitivity analysis of MHD bioconvective slip flow of nanomaterial with binary chemical reaction and Newtonian heating

Md Faisal Md Basir[1] | **Muhammad Bilal**[2] | **Rakesh Choudhary**[3] | **Joby Mackolil**[4] | **B. Mahanthesh**[4] | **Kottakkaran S. Nisar**[5]

[1]Department of Mathematical Sciences, Faculty of Science, Universiti Teknologi Malaysia, Johor Bahru, Johor, Malaysia

[2]The University of Lahore, Gujrat Campus, Gujrat, Pakistan

[3]School of General Education, Bhartiya Skill Development University, Jaipur, Rajasthan, India

[4]Department of Mathematics, CHRIST (Deemed to be University), Bangalore, Karnataka, India

[5]Department of Mathematics, College of Arts and Sciences, Prince Sattam bin Abdulaziz University, Wadi Al Dawaser, Saudi Arabia

Correspondence
B. Mahanthesh, Department of Mathematics, CHRIST (Deemed to be University), Bangalore, Karnataka 560029, India.
Email: mahanthesh.b@christuniversity.in

Abstract

The impact of Stefan blowing on the MHD bioconvective slip flow of a nanofluid towards a sheet is explored using numerical and statistical tools. The governing partial differential equations are nondimensionalized and converted to similarity equations using apposite transformations. These transformed equations are solved using the Runge–Kutta–Fehlberg method with the shooting technique. Graphical visualizations are used to scrutinize the effect of the controlling parameters on the flow profiles, skin friction coefficient, local Nusselt, and Sherwood number. Moreover, the sensitivities of the reduced Sherwood and Nusselt number to the input variables of interest are explored by adopting the response surface methodology. The outcomes of the limiting cases are emphatically in corroboration with the outcomes from preceding research. It is found that the heat transfer rate has a positive sensitivity towards the haphazard motion of the nanoparticles and a negative sensitivity towards the thermomigration. The thermal field is enhanced by the Stefan blowing aspect. Moreover, the fluid velocity can be controlled by the applied magnetic field.

KEYWORDS

Arrhenius activation energy, binary chemical reaction, bioconvection, nanofluid, Newtonian heating, response surface methodology, sensitivity analysis

1 | INTRODUCTION

As it is intricate to consider all the chemical reactions in a system, the decision to confine to only binary type seems to be progressively helpful and short-sighted. First of all, activation energy must be accessible, as it is desired by a chemical reaction. This issue can be resolved by utilizing the Arrhenius equations that depict the steady changes in the rate in temperature. It is well-known that a chemical variation describes chemical reactions, and at least one item is yielded that has properties not quite the same as the reactants. In manufacturing procedures, numerous mechanical applications require some chemical reactions as their prerequisite. These reactions are regularly conducted in chemical reactors and, more often than not, restricted by the accomplished mass transfer. Therefore, a proficient reaction must be constructed, by limiting the quantity of reagent, energy sources, and waste, while augmenting the yield.

Initially, the effect of the chemical reaction in a binary reaction model that possesses Arrhenius actuation energy was investigated by Bestman.[1] Later on, Hamid et al.,[2] in their study, have elaborated the combined impacts of unsteady variable magnetic field flow, as well as the heat source/sink on Williamson nanomaterial, which is produced by a stretching cylinder. Moreover, Khan et al.[3] studied the effects of second law analysis and binary chemical reaction under the existence of Arrhenius activation energy in an MHD radiative flow of nanomaterial. Recently, Khan et al.[4] and Dhlamini et al.[5] also elaborated the effects of boundary layer flows that exist in binary chemical reactions.

Numerous researchers and scientists are working towards the path to expanding the productivity of heat transfer phenomena of fluid dynamics, especially the fluids utilized in daily life. Bioconvection adopts an essential part in fluid mechanics, ecological framework, and modern engineering. This sort of convection is prompted because of an unstable density stratification brought about by up-swimming microorganisms. Motile microorganisms endure just in the base liquid; henceforth, the nanofluid must be water-based. Some important uses of bioconvection inorganic framework and biotechnology are, for example, bio-microsystem, chemical biosensors, mass transfer of biotechnology, and so forth. Numerous scientists have explored gyrotactic microorganisms in fluid dynamics; for example, Childress et al.[6] broke down the hypothesis of a suspension of swimming microorganisms. In this investigation, they presumed that the life form motility is characterized by a diffusivity tensor D, as well as an average upward swimming speed U. Makinde and Animasaun[7] studied MHD nanofluid flow with bioconvection and nonlinear thermal radiation, as well as the chemical reaction of quartic autocatalysis over a paraboloid of revolution's upper surface. Later on, Raju et al.,[8] Salim et al.,[9] and Khan et al.[10] addressed microorganism bioconvection under various geometries in fluid dynamics. Their inspections report that the transport of heat can enhance by utilizing the microorganism bioconvection in base fluid flow.

The Newtonian heating, or also known as the conjugate convective flow, is named as a direct proportionate amidst the neighborhood temperature and rate of heat transfer. It is important to note that the utilization of Newtonian heating is of utmost importance in numerous procedures, for example, heat exchangers, convective flow, where the sun-oriented radiators supply the heat, and so on. The four classifications of the heat transfer viz. (i) steady or endorsed surface heat flux, (ii) Newtonian heating, (iii) conjugate limit or boundary condition, as well as (iv) constant or endorsed temperature of the surface, are given by Merkin.[11]

The investigation of MHD assumes an exceptional part in the transfer of heat and mass and in regulating the momentum within the boundary layer bioconvection nanofluid flow via a stretching/shrinking surface. Moreover, the utilization of magnetohydrodynamics has been employed in designing various applications, such as the cooling of an atomic reactor, plasma restriction, as well as electromagnetic throwing. Furthermore, regarding microfluidics complexities, magnetohydrodynamics is beneficial in producing nonthrobbing and continuous movement within the structure of multiple small-scale channels. It also contributes significantly to the field of biomedical engineering, as it is relevant to magnetic drugs for cancer. Thus, acknowledging the usefulness of magnetohydrodynamics across various applications, Khan et al.[12] carried out an investigation focusing on the phenomenon of heat and mass transfer in the existence of MHD thermal and radiation thin-film second-grade fluid over a stretching sheet. In their study, the residual errors in the validation of the results were found. Also, Palwasha et al.[13] studied the thin-film fluid flow of the two-dimensional boundary layer, considering variable thermophysical properties. Their result showed that the MHD impact is a very overwhelming component of the flow. Khan et al.[14] and Zuhra et al.[15] also examined the slip flow effects of Eyring–Powell and water-based liquid nanofluid film, including graphene nanoparticles. Furthermore, Okedoye and Ogunniyi[16] studied the impacts of binary chemical reaction for MHD boundary layer flow over a moving plate. Later on, numerous researchers have discussed the MHD effects with various physical parameters and geometries.[17–20]

The investigation of boundary layer fluid flow over a shrinking/stretching sheet has picked up much interest because of its vast territory of uses in numerous industries. Wang[21] examined the stagnation point flow due to a stretching sheet. Bachok et al.[22] and Reddy and Gorla[23] also explored the effects of heat transfer, as well as stagnation point flow on a shrinking/stretching sheet.

Using statistical techniques in the analysis of the impact of a variety of parameters is a recent trend. Correlation, probable error, and regression models have been used by researchers for statistical analysis.[24–26] For this purpose, the response surface methodology (RSM) is a statistical and mathematical method employed in developing and improvising processes. Improving the present design of products can be achieved as the results of this analysis. When there are several effective parameters that affect the process, a better understanding of their sensitivities helps to modify the product. Mamourian et al.[27] explored the sensitivity of the rate of heat transfer and the drop of pressure with respect to effective parameters for a nanofluid flow in a solar heat exchanger. Moreover, the Nusselt number sensitivity to the magnetic field strength, fin angle, and fin relative thermal conductivity was investigated by Pordanjani et al.[28] using the RSM. Some explorations to study the sensitivity can be seen in References [29–31].

Motivated by the above-stated investigations, we found that there is very little or no study that was conducted that investigate the effect of MHD bioconvective flow over a stretching sheet with Arrhenius activation energy, as well as the effect of the first- and second-order slip nanofluid flow with microorganism.

2 | MATHEMATICAL FORMULATION

Consider the boundary layer flow of a nanomaterial on an elongated sheet in the free stream. The Cartesian coordinate system $(\bar{x}, \bar{y})$ is employed such that the $\bar{x}$-axis is positioned along the sheet, while the $\bar{y}$-axis is set in the direction normal to the sheet (see Figure 1). Moreover, the presence of gyrotactic microorganism and the steady flow is considered. Furthermore, the temperature, T_w and the motile microorganism density N_w are used at the boundary wall. Meanwhile, it is supposed that T_∞, C_∞, and N_∞ are their ambient values. In approximating this flow problem, a passively controlled nanofluid model is utilized. This is to make the model physically more realistic as compared to the actively controlled nanofluid models that were widely used previously. The suspended nanoparticles in the base fluid are assumed to be stable and do not influence the swimming direction and velocity of the microorganisms. Moreover, it is also in the assumption that the nanofluid is dilute, which can evade the instability of the bioconvection as the viscosity increases. On the other hand, it is required for the base fluid to be water to ensure that the microorganisms would survive. Multiple slip boundary conditions are subjected to the sheet. A magnetic field of strength B_0^2 is applied in the positive direction of $\bar{x}$-axis. The conservation of mass, momentum, thermal, energy, nanoparticles, and microorganism are, respectively, expressed in five field equations as follows:

$$\frac{\partial \bar{u}}{\partial \bar{x}} + \frac{\partial \bar{v}}{\partial \bar{y}} = 0, \tag{1}$$

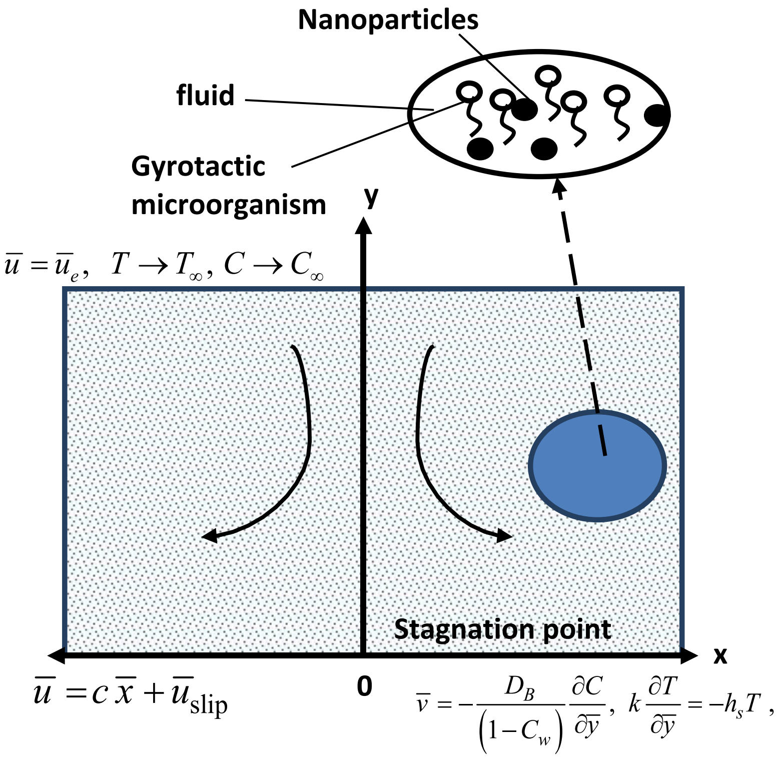

FIGURE 1 Schematic diagram of the model [Color figure can be viewed at wileyonlinelibrary.com]

$$\bar{u}\frac{\partial \bar{u}}{\partial \bar{x}} + \bar{v}\frac{\partial \bar{u}}{\partial \bar{y}} = \upsilon\frac{\partial^2 \bar{u}}{\partial \bar{y}^2} - \frac{\sigma B_0^2}{\rho}(\bar{u} - \bar{u}_e) + \bar{u}_e\frac{d\bar{u}_e}{d\bar{x}}, \tag{2}$$

$$\bar{u}\frac{\partial T}{\partial \bar{x}} + \bar{v}\frac{\partial T}{\partial \bar{y}} = \alpha\frac{\partial^2 T}{\partial \bar{y}^2} + \frac{Q_0}{\rho C_p}(T - T_\infty) + \tau D_B\frac{\partial T}{\partial \bar{y}}\frac{\partial C}{\partial \bar{y}} + \tau\left(\frac{D_T}{T_\infty}\right)\left(\frac{\partial T}{\partial \bar{y}}\right)^2, \tag{3}$$

$$\bar{u}\frac{\partial C}{\partial \bar{x}} + \bar{v}\frac{\partial C}{\partial \bar{y}} = D_B\frac{\partial^2 C}{\partial \bar{y}^2} + \left(\frac{D_T}{T_\infty}\right)\frac{\partial^2 T}{\partial \bar{y}^2} - k_r^2(C - C_\infty)\left(\frac{T}{T_\infty}\right)^m \exp\left(\frac{-E_a}{K^*T}\right), \tag{4}$$

$$\bar{u}\frac{\partial N}{\partial \bar{x}} + \bar{v}\frac{\partial N}{\partial \bar{y}} + \frac{\tilde{b}W_C}{C_\infty}\left[\frac{\partial}{\partial \bar{y}}\left(N\frac{\partial C}{\partial \bar{y}}\right)\right] = D_n\frac{\partial^2 N}{\partial \bar{y}^2}. \tag{5}$$

The boundary conditions are,

$$\begin{aligned}
&\bar{u} = c\,\bar{x} + \bar{u}_{\text{slip}},\ \bar{v} = -\frac{D_B}{(1 - C_w)}\frac{\partial C}{\partial \bar{y}},\ k\frac{\partial T}{\partial \bar{y}} = -h_s T,\\
&D_B\frac{\partial C}{\partial \bar{y}} + \frac{D_T}{T_\infty}\frac{\partial T}{\partial \bar{y}},\ N = N_w \text{ at } \bar{y} = 0,\\
&\bar{u} = \bar{u}_e,\ T \to T_\infty,\ C \to C_\infty,\ N \to 0 \text{ as } \bar{y} \to \infty.
\end{aligned} \tag{6}$$

In the above equations, υ is the kinematic viscosity, ρ is the density of the fluid, σ is the electrical conductivity, α is the thermal diffusivity, Q_0 is the variable heat generation/absorption, c_p is the specific heat at constant pressure, $\tau = (\rho c)_p/(\rho c)_f$ is the heat capacities ratio, D_B is the Brownian diffusion coefficient, D_T is the thermophoretic diffusion coefficient, k_r^2 is the rate of reaction, $\tilde{b}$ is the chemotaxis constant, W_c is the cell swimming maximum speed, D_n is the microorganisms diffusivity, $(\bar{u}, \bar{v})$ illustrate the components of velocity along $\bar{x}$- and $\bar{y}$-axis, $\bar{u}_{\text{slip}} = N_1\frac{\partial \bar{u}}{\partial \bar{y}} + N_2\frac{\partial^2 \bar{u}}{\partial \bar{y}^2}$ is the velocity slip parameter, m is fitted rate constant, E_a is the activation energy, and K^* is the Boltzmann constant.

2.1 | Nondimensionalization of the governing equations

The governing equations are expressed in dimensionless form by using the dimensionless variables as follows:

$$\begin{aligned}
&x = \frac{\bar{x}}{\sqrt{\frac{\upsilon}{a}}},\ y = \frac{\bar{y}}{\sqrt{\frac{\upsilon}{a}}},\ u = \frac{\bar{u}}{\sqrt{\upsilon a}},\ v = \frac{\bar{v}}{\sqrt{\upsilon a}},\ u_e = \frac{\bar{u}_e}{\sqrt{\upsilon a}}\\
&\theta = \frac{T - T_\infty}{T_\infty},\ \phi = \frac{C - C_\infty}{C_\infty},\ \chi = \frac{N}{N_w},
\end{aligned} \tag{7}$$

where a is a positive constant. The stream function is introduced as follows:

$$u = \frac{\partial \psi}{\partial y} \text{ and } v = -\frac{\partial \psi}{\partial x}. \tag{8}$$

Therefore, Equations (2)–(5) become:

$$\frac{\partial\psi}{\partial y}\frac{\partial^2\psi}{\partial x\partial y} - \frac{\partial\psi}{\partial x}\frac{\partial^2\psi}{\partial y^2} = \frac{\partial^3\psi}{\partial y^3} - M\left(\frac{\partial\psi}{\partial y} - u_e\right) + u_e\frac{du_e}{dx}, \tag{9}$$

$$\frac{\partial\psi}{\partial y}\frac{\partial\theta}{\partial x} - \frac{\partial\psi}{\partial x}\frac{\partial\theta}{\partial y} = \frac{1}{Pr}\frac{\partial^2\theta}{\partial y^2} + \frac{Q_0}{a\rho c_p}\theta + \frac{Nb}{Pr}\frac{\partial\theta}{\partial y}\frac{\partial\phi}{\partial y} + \frac{Nt}{Pr}\left(\frac{\partial\theta}{\partial y}\right)^2, \tag{10}$$

$$\frac{\partial\psi}{\partial y}\frac{\partial\phi}{\partial x} - \frac{\partial\psi}{\partial x}\frac{\partial\phi}{\partial y} = \frac{1}{LePr}\frac{\partial^2\phi}{\partial y^2} + \frac{Nt}{Nb}\frac{1}{LePr}\frac{\partial^2\theta}{\partial y^2} - K_E\,\phi(1+\theta)^m\,e^{\left[\frac{-E_c}{1+\theta}\right]}, \tag{11}$$

$$\frac{\partial\psi}{\partial y}\frac{\partial\chi}{\partial x} - \frac{\partial\psi}{\partial x}\frac{\partial\chi}{\partial y} + \frac{Pe}{LbPr}\left[\chi\frac{\partial^2\phi}{\partial y^2} + \frac{\partial\phi}{\partial y}\frac{\partial\chi}{\partial y}\right] = \frac{1}{LbPr}\frac{\partial^2\chi}{\partial y^2}, \tag{12}$$

with the corresponding boundary conditions as follows:

$$\begin{gathered}\frac{\partial\psi}{\partial y} = \lambda_1 x + N_1\frac{1}{\left(\sqrt{\frac{\upsilon}{a}}\right)}\frac{\partial^2\psi}{\partial y^2} + N_2\frac{a}{\upsilon}\frac{\partial^3\psi}{\partial y^3},\ \frac{\partial\psi}{\partial x} = \frac{C_\infty}{LePr(1-C_w)}\frac{\partial\phi}{\partial y},\\ \frac{\partial\theta}{\partial y} = -\frac{h_s}{k}\sqrt{\frac{a}{\upsilon}}(1+\theta),\ Nb\frac{\partial\phi}{\partial y} + Nt\frac{\partial\theta}{\partial y} = 0,\ \chi = 1 \text{ at } y = 0,\\ \frac{\partial\psi}{\partial y} = u_e,\ \theta\to 0,\ \phi\to 0, \chi\to 0 \text{ as } y\to\infty.\end{gathered} \tag{13}$$

where $Pr = \frac{\upsilon}{\alpha}$ is the Prandtl number, $M = \frac{\sigma B_0^2}{\rho a}$ is the magnetic field parameter, $Nt = \frac{\tau D_T\Delta T}{T_\infty\alpha}$ is the thermophoresis parameter, $Nb = \frac{\tau D_B C_\infty}{\alpha}$ is the Brownian motion parameter, $Le = \frac{\alpha}{D_B}$ is the Lewis number, $Pe = \frac{\tilde{b}W_c}{D_n}$ is Péclet number, $K_E = \frac{k_r^2}{a}$ is the chemical reaction parameter, $\lambda_1 = \frac{c}{a}$ is the stretching/shrinking parameter, $E_c = \frac{E_a}{K^*T_\infty}$ is the nondimensional activation energy, and $Lb = \frac{\alpha}{D_n}$ is the bioconvection Lewis number.

Next, the following transformations are employed:

$$\begin{aligned}&\eta = y,\ \psi = x\,f(\eta)\,\theta = \theta(\eta),\ \phi = \phi(\eta),\ \chi = \chi(\eta),\\ &u_e = x\end{aligned} \tag{14}$$

where, η is the independent similarity variable. We then substitute Equation (14) into Equations (9)–(13) and obtain the following equations which are ordinary differential equations (ODEs):

$$f''' + ff'' - f'^2 - M(f' - 1) + 1 = 0, \tag{15}$$

$$\theta'' + Prf\theta' + Nb\theta'\phi' + Nt\theta'^2 + PrQ\theta = 0, \tag{16}$$

$$\phi'' + PrLef\phi' + \frac{Nt}{Nb}\theta'' - PrLeK_E\phi(1+\theta)^m\exp\left(\frac{-E_c}{1+\theta}\right) = 0, \tag{17}$$

$$\chi'' + PrLbf\chi' - Pe(\chi\phi'' + \phi'\chi') = 0. \tag{18}$$

Furthermore, the boundary conditions are as follows:

$$\begin{aligned}&f'(0) = \lambda_1 + L_1 f'' + L_2 f''',\ f(0) = s_1\frac{1}{Pr\ Le}\phi',\ \theta' = -\gamma(1+\theta),\\ &Nb\ \phi' + Nt\ \theta' = 0,\ \chi(0) = 1,\ \text{at } \eta = 0,\end{aligned}$$

$$f'(\infty) = 1, \; \theta(\infty) = \phi(\infty) = \chi(\infty) = 0. \text{ as } \eta \to \infty. \tag{19}$$

Here, prime $(\,)'$ is identified as differentiation in term of η. $Q = \frac{Q_0}{\rho c_p a}$ is the heat generation/adsorption parameter, $L_1 = N_1 \frac{1}{\sqrt{\frac{\upsilon}{a}}} \geq 0$ and $L_2 = N_2 \frac{a}{\upsilon} \leq 0$ are the first-order velocity slip and second-order slip, respectively, $s_1 = \frac{C_\infty}{1 - C_w}$ is the Stefan blowing parameter, while $\gamma = \frac{h_s}{k}\sqrt{\frac{\upsilon}{a}}$ is the conjugate parameter for Newtonian heating. Note that $\lambda_1 > 0$ corresponding to a stretching and $\lambda_1 < 0$ corresponding to a shrinking, while s_1 positive for injection (blowing) and negative for suction.

2.2 | Physical quantities

The quantities related to this study's practical interest are the skin friction $C_{f_{\bar{x}}}$, Nusselt number $Nu_{\bar{x}}$, Sherwood number $Sh_{\bar{x}}$, and the motile microorganism density number $Nn_{\bar{x}}$, which are described as follows:

$$\begin{aligned} C_{f_{\bar{x}}} &= \frac{\tau_w}{\rho \bar{u}_e^2}, Nu_{\bar{x}} = \frac{-\bar{x} q_w}{k(T_w - T_\infty)}, \\ Sh_{\bar{x}} &= \frac{-\bar{x} q_m}{D_B(C_w - C_\infty)}, Nn_{\bar{x}} = \frac{-\bar{x} q_n}{D_n N_w}. \end{aligned} \tag{20}$$

In the above equations, τ_w, q_w, q_m, and q_n represent the skin friction, as well as the surface heat, mass, and motile microorganism flux. These quantities are expressed as

$$\tau_w = \mu \left(\frac{\partial \bar{u}}{\partial \bar{y}} \right)_{\bar{y}=0}, \; q_w = -k \left(\frac{\partial T}{\partial \bar{y}} \right)_{\bar{y}=0}, \; q_m = -D_B \left(\frac{\partial C}{\partial \bar{y}} \right)_{\bar{y}=0}, \; q_n = -D_n \left(\frac{\partial N}{\partial \bar{y}} \right)_{\bar{y}=0}. \tag{21}$$

Equations (7), (24), and (31) are then substituted into (30), which enables us to obtain

$$\begin{aligned} f''(0) = Re_{\bar{x}}^{1/2} C_f, \; -\frac{\theta'(0)}{\theta(0)} = Re_{\bar{x}}^{-1/2} Nu_{\bar{x}}, \\ -\frac{\phi'(0)}{\phi(0)} = Re_{\bar{x}}^{-1/2}\, Sh, \; -\chi'(0) = Re_{\bar{x}}^{-1/2} Nn_{\bar{x}}. \end{aligned} \tag{22}$$

$Re_{\bar{x}} = \frac{\bar{u}_e \bar{x}}{\upsilon}$ is the dimensional local Reynolds number.

2.3 | Numerical solution

The governing system of equations is a coupled nonlinear boundary value problem. These equations are solved by utilizing the Runge–Kutta–Fehlberg method (RKF45) together with the shooting procedure. The following substitutions are made to change higher-order nonlinear equations into a first-order ordinary differential system.

$$f = f_1, f' = f_2, f'' = f_3, f''' = f'_3, \tag{23}$$

$$\theta = f_4, \theta' = f_5, \theta'' = f'_5, \tag{24}$$

$$\phi = f_6, \phi' = f_7, \phi'' = f'_7, \tag{25}$$

$$\chi = f_8, \chi' = f_9, \chi'' = f'_9. \tag{26}$$

Using Equations (23)–(26), Equations (15)–(18) become

$$f'_3 = f_2^2 - f_1 f_3 + M(f_2 - 1) - 1, \tag{27}$$

$$f'_5 = -Pr\, f_1 f_5 - N_b f_5 f_7 - N_t f_5^2 - PrQ f_4, \tag{28}$$

$$f'_7 = -PrLe f_1 f_7 - \frac{N_t}{N_b} f'_5 + PrLeK_E f_6 (1 + f_4)^m \exp\left(\frac{-E_c}{1 + f_4}\right), \tag{29}$$

$$f'_9 = Pe[f_8 f'_7 + f_7 f_9] - PrLb\, f_1 f_9. \tag{30}$$

These quantities are subjected to boundary conditions which are

$$\begin{aligned} &f_1(0) = s_1 \tfrac{1}{PrLe} f_7,\ f_2(0) = \lambda_1 + L_1 f_3 + L_2 f'_3,\ f_3(0) = r_1, \\ &f_4(0) = -\tfrac{f_5}{\gamma} - 1,\ f_5(0) = r_2, \\ &f_7(0) = -\tfrac{N_t}{N_b} f_5,\ f_7(0) = r_3, \\ &f_8(0) = 1,\ f_9(0) = r_4, \end{aligned} \tag{31}$$

where initial guesses for $f''(0)$, $\theta'(0)$, $\phi'(0)$, and $\chi'(0)$ are r_1, r_2, r_3, and r_4, respectively. To discover these values, the Secant method is used with shooting techniques.

The RKF45 technique is considered, as a well-precise method. To obtain the solution of the initial value problem, for the computational methodology, η_∞ is rescaled to η_8 $(0 \le \eta \le 8)$. The step size is taken as $\Delta\eta = 0.001$. The method is iterated until the ideal convergence exactness of 10^{-6} is obtained.

The algorithm of this method is as follows:

$$y_{m+1} = y_m + h\left(\frac{25}{216}k_0 + \frac{1408}{2565}k_2 + \frac{2197}{4104}k_3 - \frac{1}{5}k_4\right), \tag{32}$$

$$y_{m+1} = y_m + h\left(\frac{16}{135}k_0 + \frac{6656}{12825}k_2 + \frac{28561}{56430}k_3 - \frac{9}{50}k_4 + \frac{2}{25}k_5\right), \tag{33}$$

where Equations (32) and (33) represent the fourth- and fifth-order Runge–Kutta scheme where,

$$k_0 = f(x_m, y_m), \tag{34}$$

$$k_1 = f\left(x_m + \frac{h}{4}, y_m + \frac{h\, k_0}{4}\right), \tag{35}$$

$$k_2 = f\left(x_m + \frac{3}{8}h, y_m + \left(\frac{3}{32}k_0 + \frac{9}{32}k_1\right)h\right), \tag{36}$$

$$k_3 = f\left(x_m + \frac{12}{13}h,\ y_m + \left(\frac{1932}{2197}k_0 - \frac{7200}{2197}k_1 + \frac{7296}{2197}k_2\right)h\right), \tag{37}$$

$$k_4 = f\left(x_m + h,\ y_m + \left(\frac{439}{216}k_0 - 8k_1 + \frac{3680}{513}k_2 - \frac{845}{4104}k_3\right)h\right), \tag{38}$$

$$k_5 = f\left(x_m + \frac{h}{2},\ y_m + \left(-\frac{8}{27}k_0 + 2k_1 - \frac{3544}{2565}k_2 + \frac{1859}{4104}k_3 - \frac{11}{40}k_4\right)h\right). \tag{39}$$

Furthermore, to determine the precision of the solution, the value of the local skin friction factor, $f''(0)$ are put into comparison with the results of Wang,[21] Bachok et al.,[22] and Reddy and Gireesha.[23] In Table 1, a comparison is established for the limiting case of $f''(0)$ against different values of stretching/shrinking parameters. It is observed that the code, which is used for the current study, is perfectly accurate and the results are reliable.

3 | RESULTS AND DISCUSSION

The numerical outcomes are denoted in the form of dimensionless velocity, motile microorganism density, nanoparticle volume fraction, and temperature. Moreover, in this study, the impact of pertinent parameters (like the activation energy, bioconvection Lewis number, chemical reaction parameter, heat absorption/generation, magnetic field, motile microorganism density, Newtonian heating, nanoparticle volume fraction, Stefan blowing, temperature, and velocity slip) are analyzed.

In Figures 2 and 3, the impact of first- and second-order velocity slip parameters on the velocity profile is displayed. One can observe from these figures that there is an enhancement of the velocity profile for higher values of slip parameter L_1. Usually, the fluid flow velocity is equal to the velocity of the stretching sheet, but in the slip mechanism, the flow velocity of the fluid near the sheet is not equal to the sheet velocity anymore. With increasing L_1, the sheet's velocity increases and this increment is not fully transmitted to the fluid, which resultantly reduces the boundary layer thickness. A direct proportion relation between the second-order slip parameter L_2 and the velocity profile is noted in

TABLE 1 Comparison of values $f''(0)$ for different stretching/shrinking parameter and ignoring all the other parameters

λ_1	Wang[21]	Bachok et al.[22]	Reddy and Gireesha[23]	Present
−0.25	1.40224	1.40224	1.40225	1.4022408
−0.5	1.49567	1.49566	1.49566	1.4956697
−0.75	1.48930	1.48929	1.48928	1.4892982
−1.0	1.32882	1.32881	1.32881	1.3288168
−1.1	–	1.18668	1.18668	1.1866802
−1.15	1.08223	1.08223	1.08223	1.0822311
−1.2	–	0.93247	0.93247	0.9324733

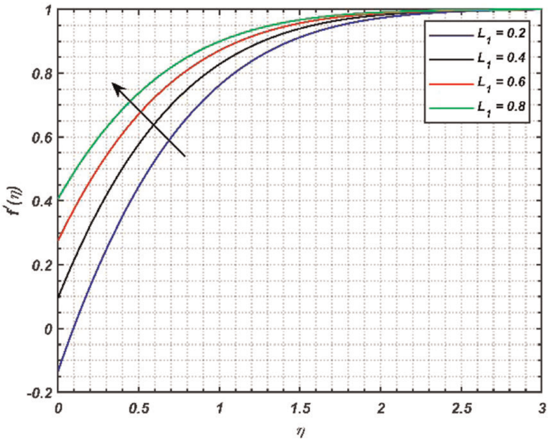

FIGURE 2 Effect of slip parameter on the velocity profile [Color figure can be viewed at wileyonlinelibrary.com]

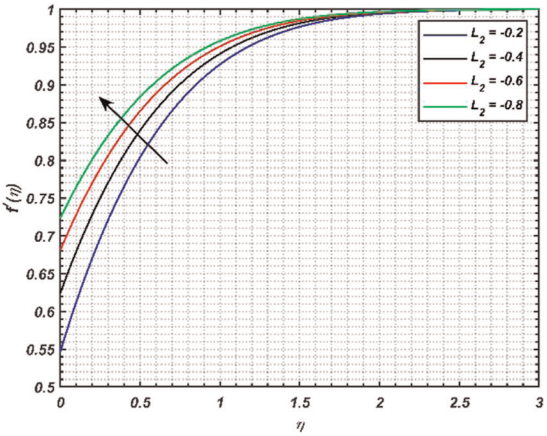

FIGURE 3 Effect of second-order slip parameter on the velocity profile [Color figure can be viewed at wileyonlinelibrary.com]

Figure 3. There is a decrease in the boundary layer thickness for the escalating values of L_2. The behavior of Biot number γ_1 is epitomized in Figure 4 for the temperature field. The graph clearly shows the mounting of temperature distribution against the augmented values of the Biot number. Mainly, the Biot number depends on the heat transfer

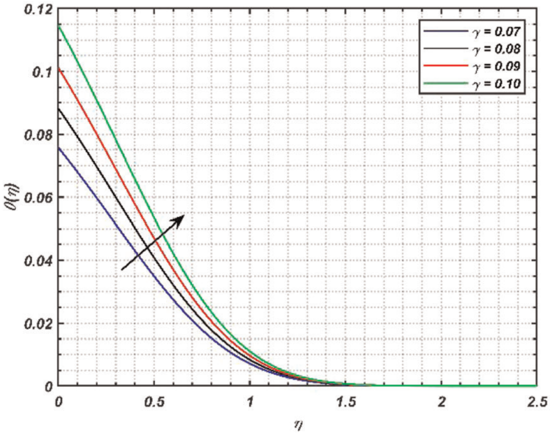

FIGURE 4 Effect of Biot number on the temperature profile [Color figure can be viewed at wileyonlinelibrary.com]

coefficient, and the increment of the heat transfer coefficient leads to an increase in the temperature and thickness of the thermal boundary layer. The effects of bioconvection Lewis number on the motile organism density profile are exhibited in Figure 5. It is also worth noting that the concentration of the motile organism is diminished when the bioconvection Lewis number is enhanced. The bioconvection Lewis number is the ratio of thermal diffusivity to the microorganism diffusivity. So, as the values of bioconvection Lewis number are incremented, the diffusivity of microorganisms is reduced, which resultantly lowers the motile organism density. The increasing values of Lewis number on nanoparticles concentration profile are plotted in Figure 6. The figure shows the decreasing trend of the concentration profile. The reason behind this fact is quite similar as described for the bioconvection Lewis number. The Lewis number is the ratio of thermal diffusivity to Brownian motion diffusivity. Therefore, the mounting values of the Lewis number reduce the Brownian motion diffusivity, which resultantly lowers the concentration profile. Next, Figure 7 presents the variation of the stretching ratio parameter λ_1 on the velocity profile. The stretching parameter is the ratio of stretching constant along the x-axis to the constant along the y-axis. One can observe from the figure that for increasing values λ_1, there is also an increment in the velocity and its associated thickness of the boundary layer.

Next, Figure 8 presents the effect of the magnetic field parameter M on the velocity profile. It is evident that the speed of flow is depreciated by the higher magnetic field parameter due to the Lorentz force. This force is usually produced for a high-strength magnetic field and is resistive. This reduction in fluid flow also reduces the thickness of the boundary layer. The applied normal magnetic field causes the resistive forces to be produced in the fluid, which consequently enhances the temperature of the fluid. This is depicted in Figure 9. On the other hand, Figure 10 demonstrates the effect of the Brownian motion parameter Nb on the concentration profile; Nb is inversely proportional to the viscosity of the fluid. The fluid becomes less viscous for the higher Brownian motion parameter, hence lower the concentration of the nanofluid. The thermophoresis parameter Nt influence on the temperature profile is exhibited in Figure 11. This figure shows the escalation of temperature against the increasing thermophoresis parameter Nt. When the parameter Nt is increased, the thermophoresis forces are enhanced, which raises the

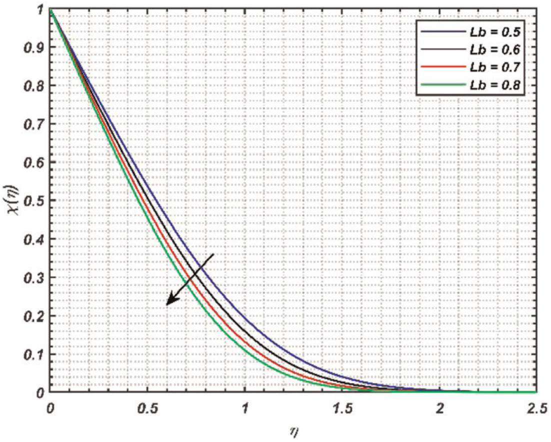

FIGURE 5 Effect of microorganism Lewis number on the motile organism density profile [Color figure can be viewed at wileyonlinelibrary.com]

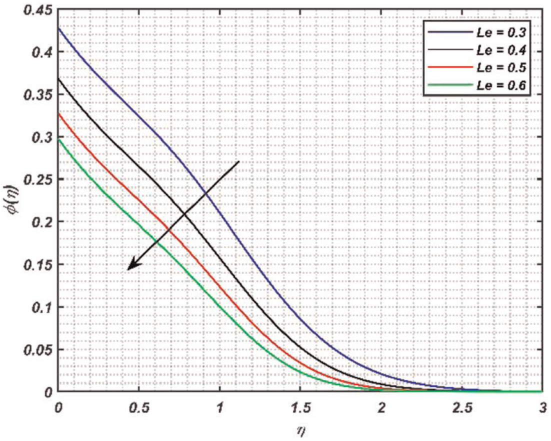

FIGURE 6 Effect of Lewis number on the concentration profile [Color figure can be viewed at wileyonlinelibrary.com]

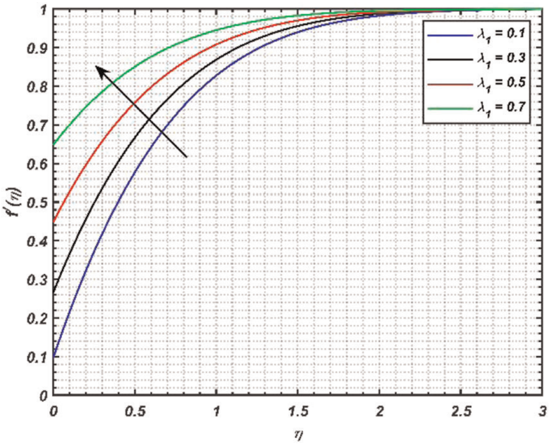

FIGURE 7 Effect of stretching ratio parameter on the velocity profile [Color figure can be viewed at wileyonlinelibrary.com]

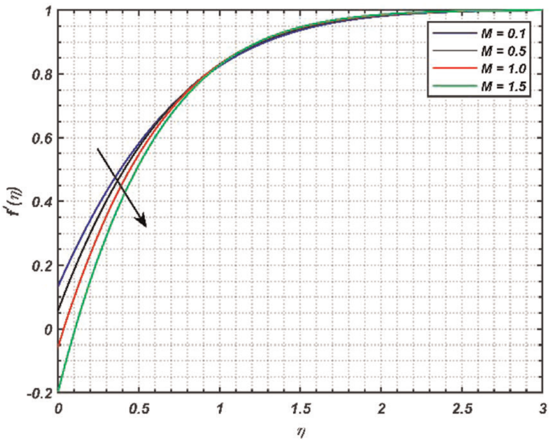

FIGURE 8 Effect of magnetic parameter on the velocity profile [Color figure can be viewed at wileyonlinelibrary.com]

nanofluid temperature. To observe the variation of Prandtl number on microorganism density profile and temperature profiles, Figures 12 and 13 are drawn. Moreover, the ratio of viscous diffusivity to thermal diffusivity is known as the Prandtl number. The thermal diffusivity decreases due to the high value of the Prandtl number. This further lowers the

FIGURE 9 Effect of magnetic parameter on the temperature profile [Color figure can be viewed at wileyonlinelibrary.com]

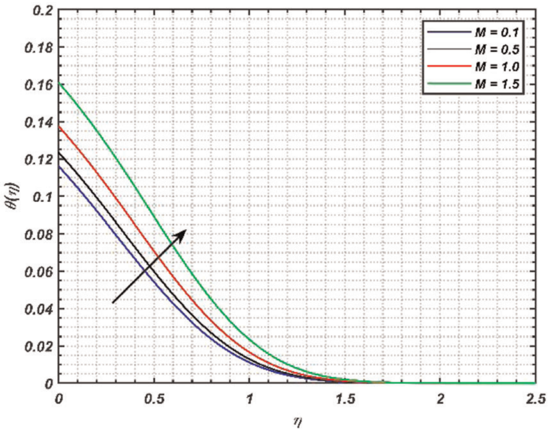

FIGURE 10 Effect of Brownian motion parameter on the concentration profile [Color figure can be viewed at wileyonlinelibrary.com]

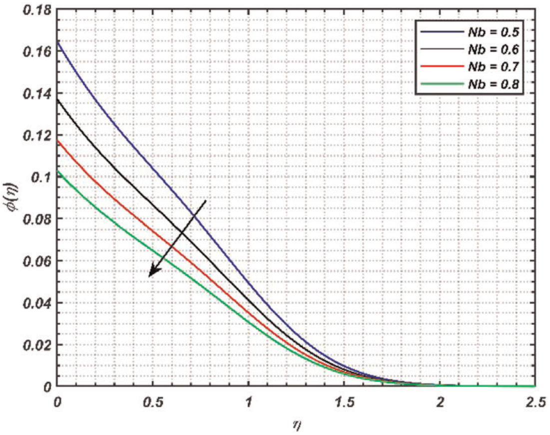

FIGURE 11 Effect of thermophoresis parameter on the temperature profile [Color figure can be viewed at wileyonlinelibrary.com]

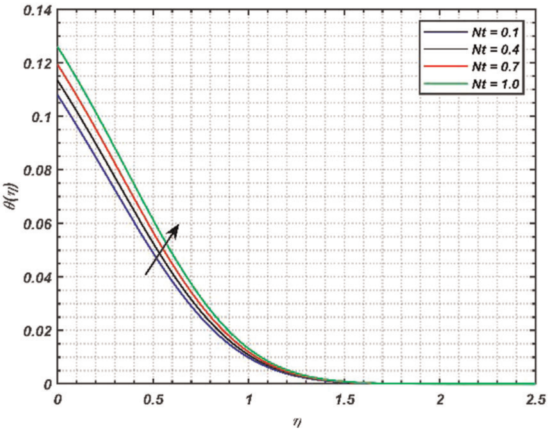

temperature of the fluid, as well as its associated thickness of the boundary layer. Also, the density of gyrotactic microorganisms is reduced for the same reasons of higher Prandtl number. Figure 14 illustrates the behavior of the heat generation parameter Q on the temperature profile. An increase in the fluid temperature is witnessed against the

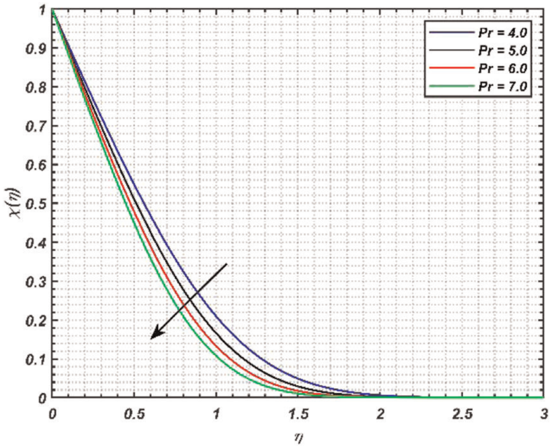

FIGURE 12 Effect of Prandtl number on the motile organism density profile [Color figure can be viewed at wileyonlinelibrary.com]

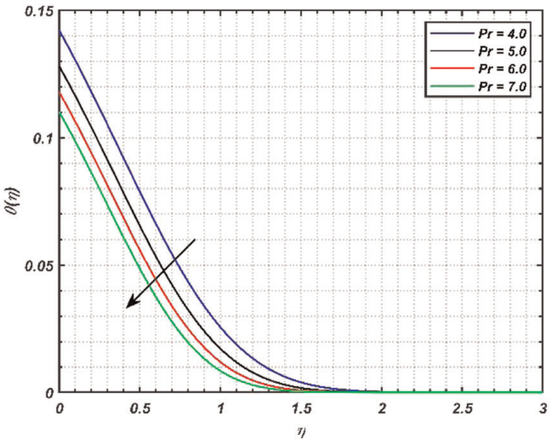

FIGURE 13 Effect of Prandtl number on the temperature profile [Color figure can be viewed at wileyonlinelibrary.com]

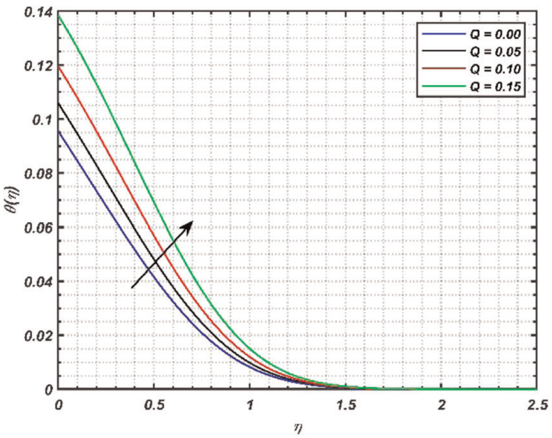

FIGURE 14 Effect of internal heat generation on the temperature profile [Color figure can be viewed at wileyonlinelibrary.com]

mounting values of Q, and this phenomenon happened due to the rapid collision of molecules with each other. The increasing Stefan blowing parameter s_1 make the fluid warmer, as depicted in Figure 15. As K_E is gradually increased, the concentration profiles become thinner (see Figure 16).

FIGURE 15 Effect of Stefan blowing parameter on the temperature profile [Color figure can be viewed at wileyonlinelibrary.com]

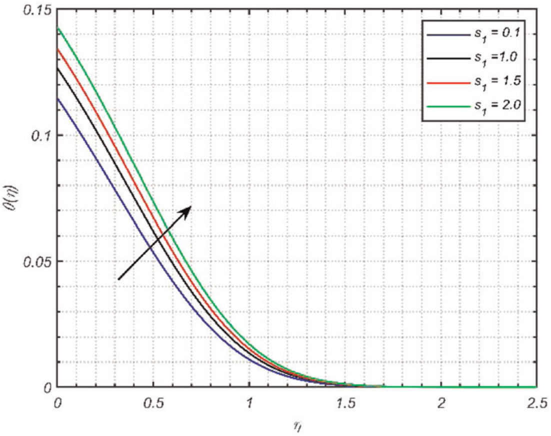

FIGURE 16 Effect of chemical reaction parameter on the temperature profile [Color figure can be viewed at wileyonlinelibrary.com]

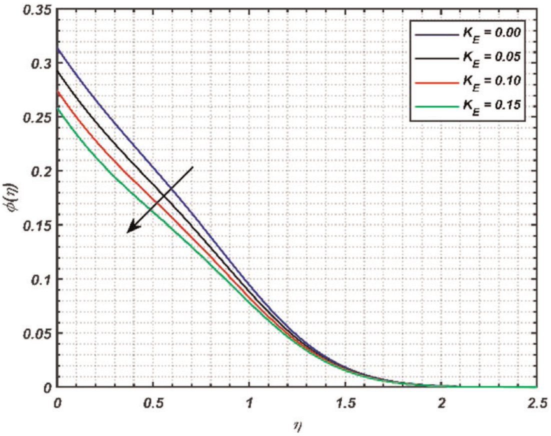

Table 2 tabulates the numerical values of the local density number of the motile gyrotactic organism, local Nusselt number, Sherwood number, as well as the skin friction coefficient for the emerging parameter, while the others are kept fixed. From the table, one can observe that the skin friction increases whereas the heat flux gradient, mass flux gradient and microorganism flux gradient decreases by increasing the magnetic field effect. A reverse relation is observed for the stretching parameter as the Nusselt, Sherwood, and density number increases for the higher stretching parameter. As Prandtl number is the ratio of viscous diffusivity to thermal diffusivity, therefore the mounting values of Prandtl number raise the Sherwood number, Nusselt number, skin friction, and the density number of the motile organism. Minor changes are observed on wall shear gradient for Pr. There is no significant impact of activation energy parameter Ec on $f''(0)$, $\frac{\theta'(0)}{\theta(0)}$, $-\chi'(0)$. But, a prominent decrement on Sherwood number is noted. The first-order velocity slip parameter L_1 has an increasing behavior on the Nusselt number and density number whereas an opposite impact on Sherwood number and skin friction coefficient is observed. The second-order velocity slip parameter L_2 shows an escalating effect on skin friction and decreasing effect on $\frac{\phi'(0)}{\phi(0)}$, $\frac{\theta'(0)}{\theta(0)}$, $-\chi'(0)$. It is observed from the table that the Biot number has a decreasing trend on skin friction and Nusselt number. Meanwhile, the Biot number has an increasing trend on the Nusselt and density number of microorganisms.

TABLE 2 Values $f''(0)$, $\frac{-\theta'(0)}{\theta(0)}(0)$, $\frac{-\phi'(0)}{\phi(0)}$, $-\chi'(0)$ when $Nb = 0.5$, $Nt = 0.5$, $Q = 0.1$, $Le = 0.7$, $K_E = 0.1$, $m = 1.0$, $Lb = 0.7$, $Pe = 0.2$, $s_1 = 0.1$

M	λ_1	Pr	E_c	L_1	L_2	γ	$f''(0)$	$\frac{-\theta'(0)}{\theta(0)}$	$\frac{-\phi'(0)}{\phi(0)}$	$-\chi'(0)$
0.3	0.1	6.2	0.3	0.4	0.4	0.1	1.2496156	0.9718936	0.9405729	1.0911774
0.4							1.3025458	0.9586078	0.9398293	1.0821846
0.5							1.3570045	0.9445221	0.9391606	1.0726479
0.6							1.4130874	0.9296205	0.9386083	1.0625584
	0.2						1.1597944	1.0584779	0.9545055	1.1511649
	0.3						1.0609717	1.1448160	0.9726400	1.2115868
	0.4						0.9522760	1.2312048	0.9940367	1.2726164
		3.0					1.2473813	0.7349522	0.6894401	0.8216107
		4.0					1.2484785	0.8230257	0.7794617	0.9197629
		5.0					1.2491236	0.8965065	0.8575744	1.0035139
			0.4				1.2496156	0.9716592	0.9303098	1.0911232
			0.5				1.2496155	0.9714402	0.9209381	1.0910726
			0.6				1.2496155	0.9712361	0.9123820	1.0910255
				+0.1			1.5688318	0.5530891	0.9892849	0.8118171
				+0.2			1.4672124	0.7132967	0.9088796	0.9164010
				+0.3			1.3584366	0.8527101	0.9002472	1.0099822
					−0.3		0.6397753	1.4430113	1.0353797	1.4247299
					−0.2		0.6987254	1.4062735	1.0233295	1.3981761
					−0.1		0.7668827	1.3620620	1.0092224	1.3663376
						0.1	1.2496156	0.9718936	0.9405729	1.0911774
						0.2	1.2470460	0.8846905	0.9622127	1.1034356
						0.3	1.2428441	0.7505640	1.0808731	1.1273481

4 | RESPONSE SURFACE METHODOLOGY

The interactive effects of Le, Nb, and Nt (factor variables) are analyzed using RSM. The reduced Nusselt (Nu_x) and Sherwood number (Sh_x) are the response variables for the face-centered Central Composite Design. Table 3 presents the factor variables as well as their three levels. Box and Wilson[32] proposed a quadratic expression for the response variable, which accounts for linear, interaction, and squared terms. The model is given below:

$$\text{Response} = b_1A^2 + b_2B^2 + b_3C^2 + b_4AB + b_5BC + b_6AC + b_7A + b_8B + b_9C + b_{10}$$

where, A, B, and C are the coded values and b_i denote the regression coefficients.

The experimental design and responses for twenty runs are tabulated in Table 4.

TABLE 3 Levels of the parameters

Parameter	Symbol	Level		
		−1 (Low)	0 (Medium)	1 (High)
Le	*A*	1	3	5
Nb	*B*	0.1	0.3	0.5
Nt	*C*	0.1	0.3	0.5

4.1 | Accuracy of the model

The ANOVA table in Table 5 can be used to evaluate the accuracy of the model. Recall that a parameter is considered significant if its p value is less than 0.05. In the model of Nu_x (see Table 5), only the square terms of Nb and Nt are not significant as their p values are more than

TABLE 4 Responses and experimental design

Runs	Coded terms			Real terms			Responses	
	A	*B*	*C*	*Le*	*Nb*	*Nt*	Nu_x	Sh_x
1	−1	−1	−1	1	0.1	0.1	1.1655940	1.289525
2	1	−1	−1	5	0.1	0.1	1.3195283	0.729514
3	−1	1	−1	1	0.5	0.1	1.1706387	1.304618
4	1	1	−1	5	0.5	0.1	1.4267878	0.938637
5	−1	−1	1	1	0.1	0.5	1.1421976	1.217627
6	1	−1	1	5	0.1	0.5	0.9812385	0.105407
7	−1	1	1	1	0.5	0.5	1.1669583	1.291043
8	1	1	1	5	0.5	0.5	1.3337405	0.736164
9	−1	0	0	1	0.3	0.3	1.1663254	1.290398
10	1	0	0	5	0.3	0.3	1.3267782	0.733078
11	0	−1	0	3	0.1	0.3	1.2282723	0.861138
12	0	1	0	3	0.5	0.3	1.3482836	1.128865
13	0	0	−1	3	0.3	0.1	1.3595189	1.160159
14	0	0	1	3	0.3	0.5	1.2974458	1.005591
15	0	0	0	3	0.3	0.3	1.3278489	1.080662
16	0	0	0	3	0.3	0.3	1.3278489	1.080662
17	0	0	0	3	0.3	0.3	1.3278489	1.080662
18	0	0	0	3	0.3	0.3	1.3278489	1.080662
19	0	0	0	3	0.3	0.3	1.3278489	1.080662
20	0	0	0	3	0.3	0.3	1.3278489	1.080662

TABLE 5 ANOVA table for (A) Nu_x and (B) Sh_x

Source	Degrees of freedom	Adjusted sum of squares	Adjusted mean square	F Value	p Value	
(A) Nu_x						
Model	9	0.20414	0.022682	25.91	0	Significant
Linear	3	0.097468	0.032489	37.11	0	Significant
Le	1	0.033219	0.033219	37.95	0	Significant
Nb	1	0.037159	0.037159	42.45	0	Significant
Nt	1	0.027091	0.027091	30.95	0	Significant
Square	**3**	0.05436	0.01812	20.7	0	Significant
$Le \times Le$	1	0.017257	0.017257	19.71	.001	Significant
$Nb \times Nb$	1	0.003865	0.003865	4.42	.062	Not significant
$Nt \times Nt$	1	0.00002	0.00002	0.02	.882	Not significant
Interaction	3	0.052311	0.017437	19.92	0	Significant
$Le \times Nb$	1	0.023108	0.023108	26.4	0	Significant
$Le \times Nt$	1	0.020428	0.020428	23.34	.001	Significant
$Nb \times Nt$	1	0.008775	0.008775	10.02	.01	Significant
Error	10	0.008754	0.000875			
Lack-of-fit	5	0.008754	0.001751	*	*	
Pure error	5	0	0			
Total	19	0.212893				
$R^2 = 95.89\%$; adjusted $R^2 = 92.19\%$						
(B) Sh_x						
Model	9	1.4852	0.165022	72.66	0	Significant
Linear	3	1.24935	0.416449	183.38	0	Significant
Le	1	0.99251	0.992509	437.03	0	Significant
Nb	1	0.14307	0.14307	63	0	Significant
Nt	1	0.11377	0.113768	50.1	0	Significant
Square	3	0.06783	0.022609	9.96	.002	Significant
$Le \times Le$	1	0.01005	0.010052	4.43	.062	Not significant
$Nb \times Nb$	1	0.01639	0.016388	7.22	.023	Significant
$Nt \times Nt$	1	0.00031	0.000314	0.14	.718	Not significant

TABLE 5 (Continued)

Source	Degrees of freedom	Adjusted sum of squares	Adjusted mean square	F Value	p Value	
Interaction	3	0.16802	0.056007	24.66	0	Significant
$Le \times Nb$	1	0.07057	0.07057	31.07	0	Significant
$Le \times Nt$	1	0.06865	0.068655	30.23	0	Significant
$Nb \times Nt$	1	0.02879	0.028795	12.68	.005	Significant
Error	10	0.02271	0.002271			
Lack-of-fit	5	0.02271	0.004542	*	*	
Pure error	5	0	0			
Total	19	1.50791				
$R^2 = 98.49\%$; adjusted $R^2 = 97.14\%$						

0.05. Therefore, they are removed from the model. Similarly, in the model for Sh_x, the square terms of Le and Nt are removed from the model (as they are not significant). The coefficient of determination (R^2) is a measure that describes the percentage of variation in the response variable that can be explained by the predictor variables. Here, using the factor variables in the models, it is possible to explain 95.89% of the variation in Nu_x and 98.49% of the variation in Sh_x. The high R^2 values add to the accuracy of the regression models. Further validation is done using the residual plots in Figure 17. The data points in the normal probability plots for both models are aligned along the straight line, which indicates the normality of the data. In addition, it can be observed that the highest deviation in the residual against fitted values plots is 0.05 for both models. All these suggest that the model is a good fit, and hence the RSM model is valid and accurate. Using the regression coefficients (see Table 6), the following multiple linear regression equations are obtained:

$$\begin{aligned} Nu_x = {} & 1.327 + 0.05764Le + 0.06096Nb - 0.05205Nt - 0.0792Le \times Le + 0.0537Le \times Nb \\ & - 0.0505Le \times Nt + 0.0331Nb \times Nt. \end{aligned} \tag{40}$$

$$\begin{aligned} Sh_x = {} & 1.0773 - 0.315Le + 0.1196Nb - 0.1067Nt - 0.0772Nb \times Nb + 0.0939Le \times Nb \\ & - 0.0926Le \times Nt + 0.06Nb \times Nt. \end{aligned} \tag{41}$$

4.2 | Statistical interpretations

The interactive effects of the factor variables (Le, Nb, and Nt) on the response variables (Nu_x and Sh_x) are visualized in Figures 18 and 19 using surface and contour plots. Moreover, the impact of two factors is determined by keeping the third factor at the medium level. Figure 18A shows the interaction of Le and Nb on Nu_x. It can be observed that the high level of both Le and Nb leads to the highest rate of heat transfer. The impacts of Le and Nt on Nu_x is given in Figure 18B. The higher level of Le ($Le = 5$) and the lower level of Nt ($Nt = 0.5$) leads to the highest Nu_x. Figure 18C displays the interactive effect of Nb and Nt on Nu_x. The increase in Nt has a decreasing impact on Nu_x, whereas Nb has an increasing impact.

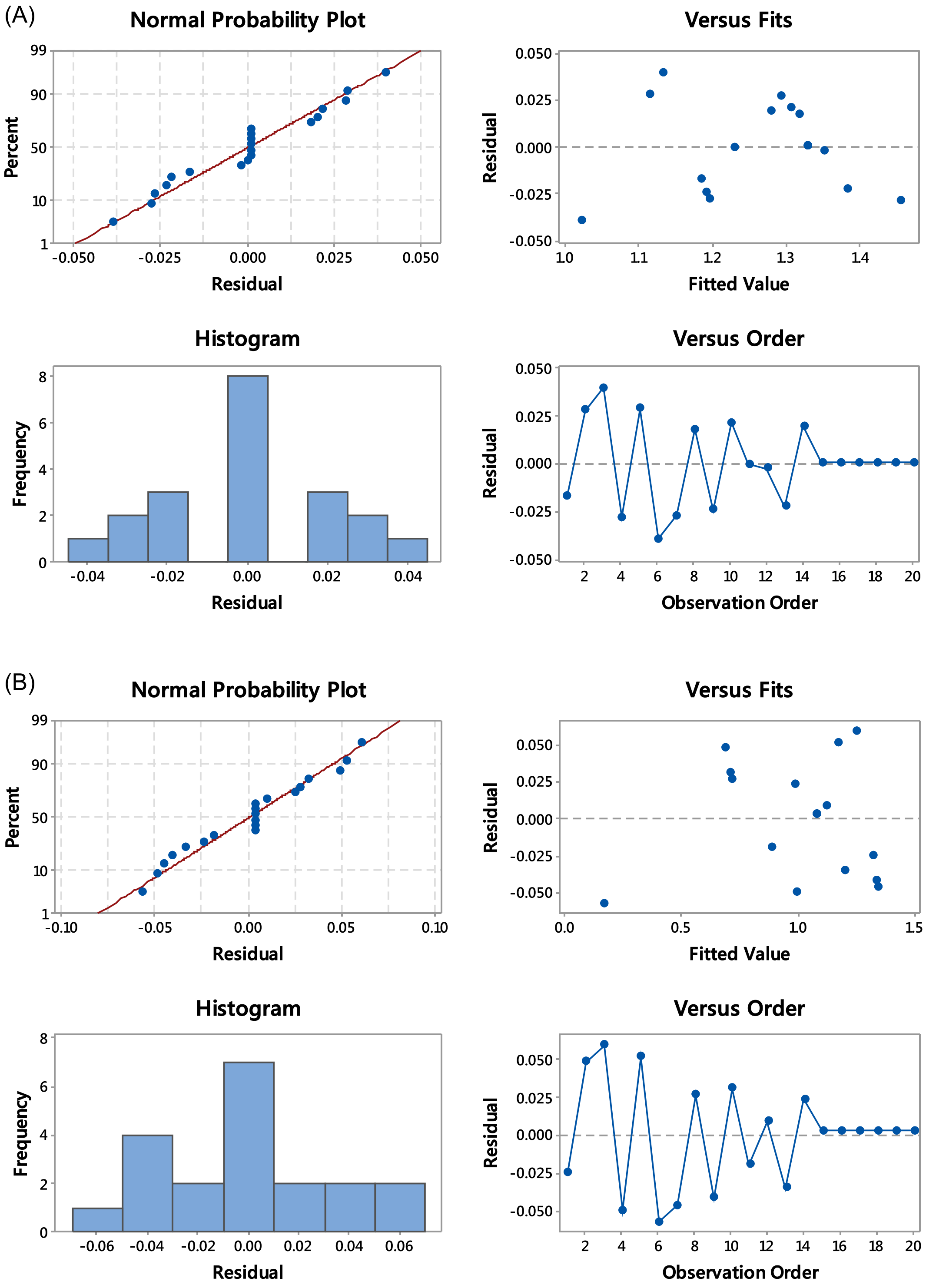

FIGURE 17 Residual Plots for (A) Nu_x and (B) Sh_x [Color figure can be viewed at wileyonlinelibrary.com]

TABLE 6 Regression coefficients of the RSM model for (A) Nu_x and (B) Sh_x

Term	Coefficient	*p* Value	
(A) Nu_x			
Constant	1.327	0	Significant
Le	0.05764	0	Significant
Nb	0.06096	0	Significant
Nt	−0.05205	0	Significant
$Le \times Le$	−0.0792	.001	Significant
$Nb \times Nb$	−0.0375	.062	Not significant
$Nt \times Nt$	0.0027	.882	Not significant
$Le \times Nb$	0.0537	0	Significant
$Le \times Nt$	−0.0505	.001	Significant
$Nb \times Nt$	0.0331	.01	Significant
(B) Sh_x			
Constant	1.0773	0	Significant
Le	−0.315	0	Significant
Nb	0.1196	0	Significant
Nt	−0.1067	0	Significant
$Le \times Le$	−0.0605	.062	Not significant
$Nb \times Nb$	−0.0772	.023	Significant
$Nt \times Nt$	0.0107	.718	Not significant
$Le \times Nb$	0.0939	0	Significant
$Le \times Nt$	−0.0926	0	Significant
$Nb \times Nt$	0.06	.005	Significant

Abbreviation: RSM, response surface methodology.

The impact of the factor variables on the reduced Sherwood number is visualized in Figure 19. The interactive effect of Le and Nb is displayed in Figure 19A. The highest reduced Sherwood number is observed when Le is at the low level for all levels of Nb. We can observe from Figure 19B that the highest reduced Sherwood number is when both Le and Nt are at the low level ($Le = 3$ and $Nt = 0.1$). Figure 19C shows that the reduced Nusselt number decreases as Nt increases. It is worth mentioning that when Le is at the medium level, the highest Sh_x is observed when Nt is at the low level ($Nt = 0.1$) and Nb is between medium and high level ($Nb = 0.4$).

5 | SENSITIVITY ANALYSIS

Next, we carry out a sensitivity analysis based on the RSM model. The partial derivatives of Nu_x and Sh_x with respect to the factor variables are called the sensitivity functions. The sensitivity functions for Nu_x are:

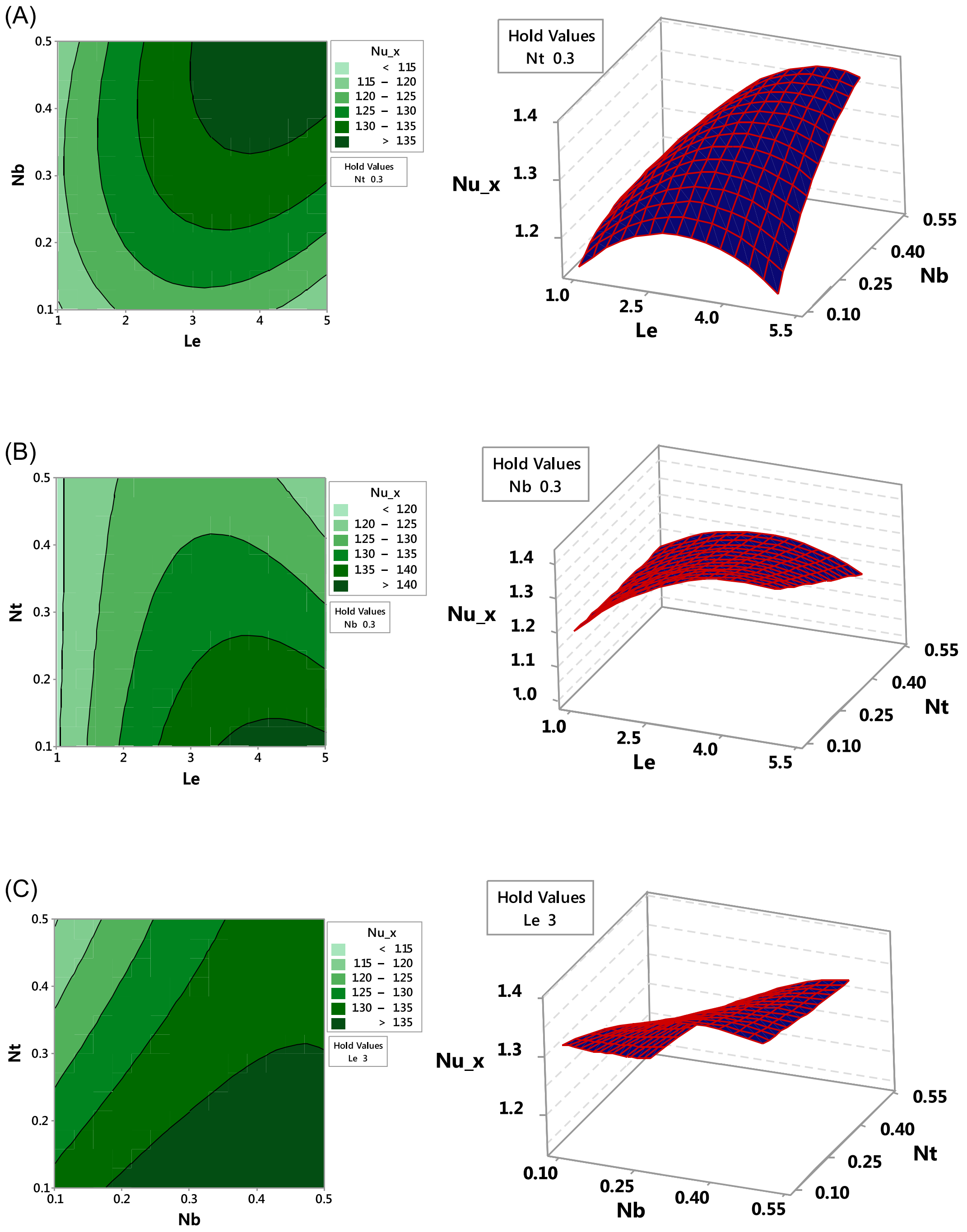

FIGURE 18 Contour plots and three-dimensional plots of reduced Nusselt number with respect to all combinations of the factor variables [Color figure can be viewed at wileyonlinelibrary.com]

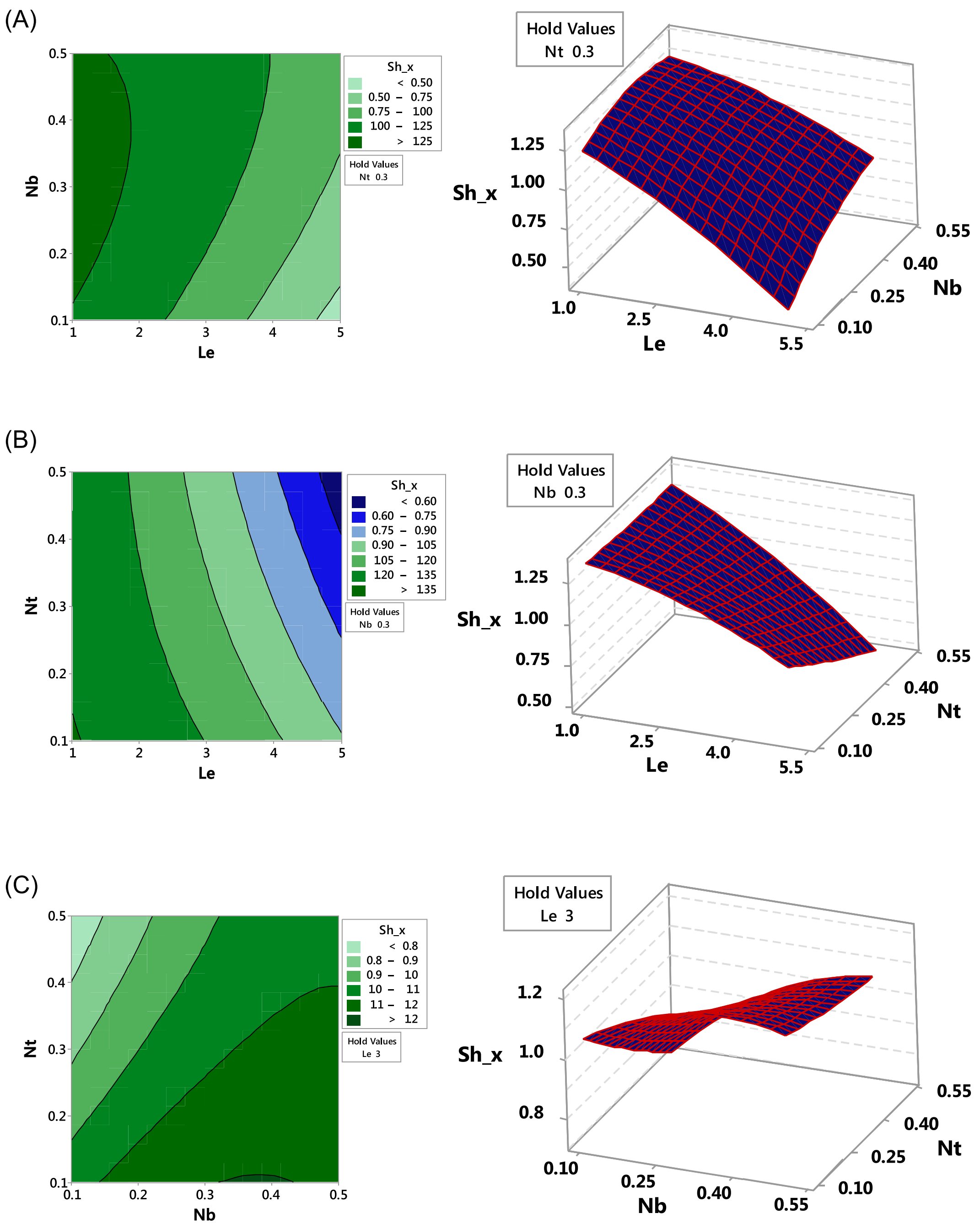

FIGURE 19 Contour plots and three-dimensional plots of reduced Sherwood number with respect to all combinations of the factor variables [Color figure can be viewed at wileyonlinelibrary.com]

$$\frac{\partial Nu_x}{\partial A} = 0.05764 - 0.1584A + 0.0537B - 0.0505C, \tag{42}$$

$$\frac{\partial Nu_x}{\partial B} = 0.06096 + 0.0537A + 0.0331C, \tag{43}$$

$$\frac{\partial Nu_x}{\partial C} = -0.05205 - 0.0505A + 0.0331B. \tag{44}$$

The sensitivity functions for Sh_x are:

$$\frac{\partial Sh_x}{\partial A} = -0.315 + 0.0939B - 0.0926C, \tag{45}$$

$$\frac{\partial Sh_x}{\partial B} = 0.1196 + 0.0939A - 0.1544B + 0.06C, \tag{46}$$

$$\frac{\partial Sh_x}{\partial C} = -0.1067 - 0.0926A + 0.06B. \tag{47}$$

The sensitivities of the response variables are given in Table 7 in keeping the medium level of the Lewis parameter (*Le*). A positive sensitivity of the response variable to a parameter signifies that the increase in that parameter leads to the increase in the response variable and vice versa. We can say that the longer the bar, the higher is the impact of it on the response variable.

From Table 7 and Figure 20, it can be concluded that Nu_x has a positive sensitivity towards *Nb* and a negative sensitivity towards *Nt*. When *Nb* is at the low level (see Figure 20A), the sensitivity of Nu_x towards *Le* decreases and the sensitivity towards *Nb* increases as the level of *Nt* is incremented from low to high. Also, the sensitivity of Nu_x towards *Nt* does not change when the level of *Nt* is incremented. It is worth mentioning that the sensitivity of Nu_x towards *Le* becomes negative when *Nt* is at the high level ($Nt = 0.5$). Nu_x has the highest positive sensitivity towards *Le* when *Nt* is in the low level and when *Nt* is in the medium, as well as high level ($Nt = 0.3$ and $Nt = 0.5$) the highest positive sensitivity is towards *Nb*. Similar trends of

TABLE 7 Sensitivity of the responses when $A = 0$

		Sensitivity					
B	***C***	$\frac{\partial Nu_x}{\partial A}$	$\frac{\partial Nu_x}{\partial B}$	$\frac{\partial Nu_x}{\partial C}$	$\frac{\partial Sh_x}{\partial A}$	$\frac{\partial Sh_x}{\partial B}$	$\frac{\partial Sh_x}{\partial C}$
−1	−1	0.054440	0.02786	−0.08515	−0.3163	0.214	−0.1667
−1	0	0.003940	0.06096	−0.08515	−0.4089	0.274	−0.1667
−1	1	−0.046560	0.09406	−0.08515	−0.5015	0.334	−0.1667
0	−1	0.108140	0.02786	−0.05205	−0.2224	0.0596	−0.1067
0	0	0.057640	0.06096	−0.05205	−0.315	0.1196	−0.1067
0	1	0.007140	0.09406	−0.05205	−0.4076	0.1796	−0.1067
1	−1	0.161840	0.02786	−0.01895	−0.1285	−0.0948	−0.0467
1	0	0.111340	0.06096	−0.01895	−0.2211	−0.0348	−0.0467
1	1	0.060840	0.09406	−0.01895	−0.3137	0.0252	−0.0467

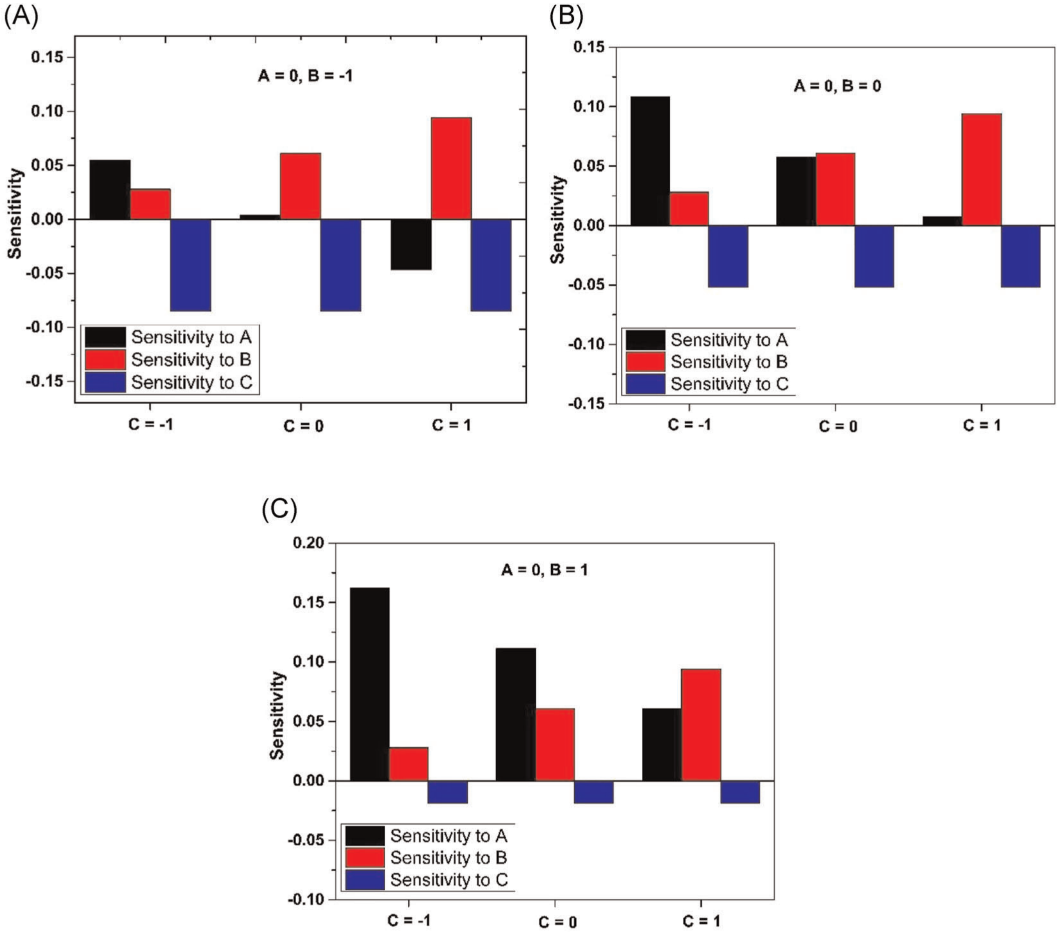

FIGURE 20 Sensitivities of Nu_x [Color figure can be viewed at wileyonlinelibrary.com]

sensitivity are also seen when Nb is at the medium level (refer to Figure 20B). However, the decrease in the positive sensitivity of Nu_x towards Le does not make it negatively sensitive. In Figure 20C, when $Nb = 0.5$ (high level), the trends are similar to the previous cases. Comparing the all bar plots in Figure 20, it can be noted that the sensitivity of Nu_x towards Le increases, whereas the sensitivity towards Nt decreases as the level of Nb is increased from a low to a high level ($Nb = 0.1$ to $Nb = 0.5$). Also, the sensitivity of Nu_x towards Nb remains unaffected to the change in the levels of Nb.

From Table 7 and Figure 21, it can be concluded that Sh_x has a negative sensitivity towards Le and Nt for all levels of Nb. When Nb is in the low level ($Nb = 0.1$), the negative sensitivity of Sh_x towards Le increases and the positive sensitivity of Sh_x towards Nb increases as the level of Nt increases from low to high. Also, the sensitivity of Sh_x towards Nt remains unaffected to the increment in the level of Nt (see Figure 21A). Similar conclusions can be drawn from Figure 21B,C. In Figure 21C, when Nb is at the high level, it can be noted that the sensitivity of Sh_x toward Nb is negative, considering the low and medium level of Nt and becomes positive for the high level of Nt (when $Nt = 0.5$).

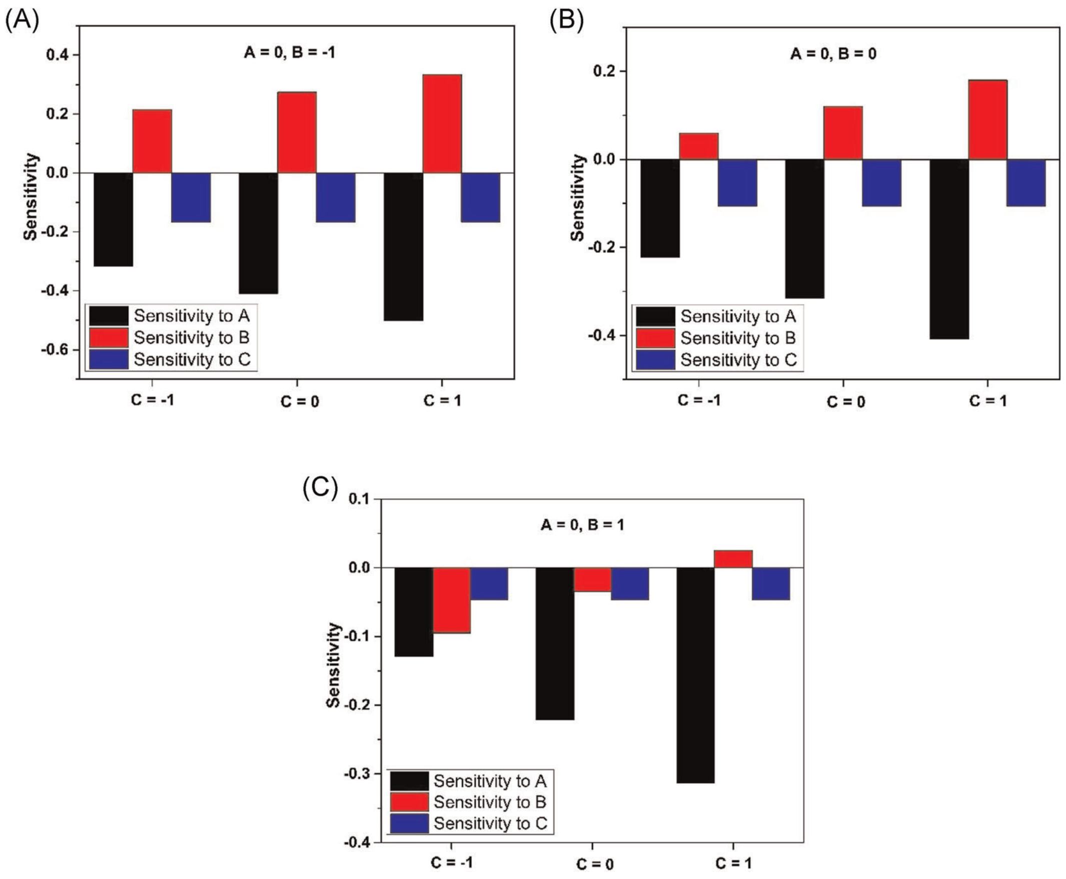

FIGURE 21 Sensitivities of Sh_x [Color figure can be viewed at wileyonlinelibrary.com]

6 | CONCLUSION

In this study, the Stefan blowing effects on the MHD bioconvective slip flow of a nanofluid over a stretching sheet is investigated numerically. The methodology involves the transformation of the microorganism, momentum, and nanoparticle volume fraction equations (partial differential equations) into a set of ODEs before they are numerically solved. Then, the numerical results obtained are put into comparison with the published results considering some limiting cases. Furthermore, a sensitivity analysis for the reduced Nusselt and Sherwood number is executed. Therefore, based on the results obtained, one can conclude that:

- The Stefan blowing parameter is responsible for the increment of the temperature profile.
- The motile organism density is reduced for the higher bioconvection Lewis number.
- The magnetic parameter has a crucial role in controlling the speed of the fluid, as the stronger magnetic field lowers the fluid velocity.
- Reduction in temperature profile is noted by incrementing the Prandtl number.
- The density number of motile microorganisms increases for the higher values of the first-order slip parameter.

- The reduced Nusselt number has a positive sensitivity toward the Brownian motion parameter and a negative sensitivity toward the thermophoresis parameter.
- The reduced Sherwood number possesses a negative sensitivity toward the Lewis number and the thermophoresis parameter.

ORCID

Md Faisal Md Basir http://orcid.org/0000-0001-5199-2693
Muhammad Bilal http://orcid.org/0000-0002-3807-0034
Rakesh Choudhary http://orcid.org/0000-0002-0413-2479
Joby Mackolil https://orcid.org/0000-0003-4829-5381
B. Mahanthesh http://orcid.org/0000-0003-2481-3842
Kottakkaran S. Nisar http://orcid.org/0000-0001-5769-4320

REFERENCES

1. Bestman AR. Radiative heat transfer to flow of a combustible mixture in a vertical pipe. *Int J Energy Res*. 1991;15:179-184.
2. Hamid A, Hashim, Khan M. Impacts of binary chemical reaction with activation energy on unsteady flow of magneto-Williamson nanofluid. *J Mol Liq*. 2018;262:435-442.
3. Khan MI, Qayyuma S, Hayat T, Waqasa M, Khan MI, Alsaedi A. Entropy generation minimization and binary chemical reaction with Arrhenius activation energy in MHD radiative flow of nanomaterial. *J Mol Liq*. 2018;259(1):274-283. https://doi.org/10.1016/j.molliq.2018.03.049
4. Khan WA, Sultan F, Ali M, Shahzad M, Khan M, Irfan M. Consequences of activation energy and binary chemical reaction for 3D flow of cross-nanofluid with radiative heat transfer. *J Braz Soc Mech Sci Eng*. 2019;41:4. https://doi.org/10.1007/s40430-018-1482-0
5. Dhlamini M, Kameswaran PK, Sibanda P, Motsa S, Mondal H. Activation energy and binary chemical reaction effects in mixed convective nanofluid flow with convective boundary conditions. *J Comput Des Eng*. 2019;6:149-158.
6. Childress S, Levandowsky M, Spiegel EA. Pattern formation in a suspension of swimming microorganisms: equations and stability theory. *J Fluid Mech*. 1975;69:591-613.
7. Makinde OD, Animasaun IL. Bioconvection in MHD nanofluid flow with non-linear thermal radiation and quartic autocatalysis chemical reaction past an upper surface of a paraboloid of revolution. *Int J Therm Sci*. 2016;109:159-171.
8. Raju CSK, Hoque MM, Sivasankar T. Radiative flow of Casson fluid over a moving wedge filled with gyrotactic microorganisms. *Adv Powder Technol*. 2017;28:575-583.
9. Saleem S, Rafiq H, Al-Qahtani A, El-Aziz MA, Malik MY, Animasaun IL. Magneto Jeffrey nanofluid bioconvection over a rotating vertical cone due to gyrotactic microorganism. *Math Probl Eng*. 2019;2019:3478037. https://doi.org/10.1155/2019/3478037
10. Khan WA, Rashad AM, Abdouc MMM, Tlili I. Natural bioconvection flow of a nanofluid containing gyrotactic microorganisms about a truncated cone. *European Journal of Mechanics - B/Fluids*. 2019;75:133-142.
11. Merkin JH. Natural-convection boundary-layer flow on a vertical surface with Newtonian heating. *Int J Heat Fluid Flow*. 1994;15:392-398.
12. Khan NS, Gul T, Islam S, Khan W. Thermophoresis and thermal radiation with heat and mass transfer in a magnetohydrodynamic thin film second-grade fluid of variable properties past a stretching sheet. *Eur Phys J Plus*. 2017;2017:132.
13. Palwasha Z, Khan NS, Shah Z, Islam S, Bonyah E. Study of two-dimensional boundary layer thin film fluid flow with variable thermophysical properties in three dimensions space. *AIP Adv*. 2018;8:105318.
14. Khan NS, Zuhra S, Shah Z, Bonyah E, Khan W, Islam S. Slip flow of Eyring-Powell nanoliquid film containing graphene nanoparticles. *AIP Adv*. 2018;8:115302.
15. Zuhra S, Khan NS, Khan MA, Islam S, Khan W, Bonyah E. Flow and heat transfer in water based liquid film fluids dispensed with graphene nanoparticles. *Results Phys*. 2018;8:1143-1157.

16. Okedoye AM, Ogunniy PO. MHD boundary layer flow past a moving plate with mass transfer and binary chemical reaction. *J Nigerian Math Soc*. 2019;38(1):89-121.
17. Krishna CM, ViswanathaReddy G, Souayeh B, Raju CSK, Gorji MR, Raju SRK. Thermal convection of MHD Blasius and Sakiadis flow with thermal convective conditions and variable properties. *Microsyst Technol*. 2019;25:3735-3746. https://doi.org/10.1007/s00542-019-04353-y
18. Ahmed N, Ali Shah N, Ahmad B, Shah SIA, Ulhaq S, Rahimi-Gorji M. Transient MHD convective flow of fractional nanofluid between vertical plates. *J Appl Comput Mech*. 2019;5(4):592-602. https://doi.org/10.22055/jacm.2018.26947.1364
19. Anjali Devi SP, Suriyakumar P. Effect of magnetic field on Blasius and Sakiadis flow of nanofluids past an inclined plate. *J Taibah Univ Sci*. 2017;11:1275-1288.
20. Jain S, Choudhary R. Dufour-Soret and thermophoretic effects on MHD mixed convection Casson fluid flow over a moving wedge and non-uniform heat source/sink. *Int J Fluid Mech Res*. 2018;45(1):51-74.
21. Wang CY. Stagnation flow towards a shrinking sheet. *Int J Nonlinear Mech*. 2008;43:377-382.
22. Bachok N, Ishak A, Pop I. Melting heat transfer in boundary layer stagnation-point flow towards a stretching/shrinking sheet. *Phys Lett A*. 2010;374:4075-4079.
23. Reddy RSG, Gireesha BJ. Dual solutions for stagnation-point flow and convective heat transfer of a Williamson nanofluid past a stretching/shrinking sheet. *Heat Mass Transf*. 2015;52:1153-1162. https://doi.org/10.1007/s00231-015-1627-y
24. Hayat T, Khan MI, Qayyum S, Alsaedi A. Modern developments about statistical declaration and probable error for skin friction and Nusselt number with copper and silver nanoparticles. *Chin J Phys*. 2017;55(6):2501-2513.
25. Mackolil J, Mahanthesh B. Time-dependent nonlinear convective flow and radiative heat transfer of Cu-Al_2O_3-H_2O hybrid nanoliquid with polar particles suspension: a statistical and exact analysis. *BioNanoScience*. 2019;9:937-951.
26. Qayyum S, Khan MI, Hayat T, Alsaedi A. A framework for nonlinear thermal radiation and homogeneous-heterogeneous reactions flow based on silver-water and copper-water nanoparticles: a numerical model for probable error. *Results Phys*. 2017;7:1907-1914.
27. Mamourian M, Shirvan KM, Mirzakhanlari S. Two phase simulation and sensitivity analysis of effective parameters on turbulent combined heat transfer and pressure drop in a solar heat exchanger filled with nanofluid by response surface methodology. *Energy*. 2016;109:49-61.
28. Pordanjani AH, Vahedi SM, Rikhtegar F, Wongwises S. Optimization and sensitivity analysis of magneto-hydrodynamic natural convection nanofluid flow inside a square enclosure using response surface methodology. *J Therm Anal Calorim*. 2019;135(2):1031-1045.
29. Vahedi SM, Pordanjani AH, Raisi A, Chamkha AJ. Sensitivity analysis and optimization of MHD forced convection of a Cu-water nanofluid flow past a wedge. *Eur Phys J Plus*. 2019;134(3):124.
30. Chan SQ, Aman F, Mansur S. Bionanofluid flow through a moving surface adapting convective boundary condition: sensitivity analysis. *J Adv Res Fluid Mech Therm Sci*. 2019;54(1):57-69.
31. Mirzakhanlari S, Shirvan KM, Mamourian M, Chamkha AJ. Increment of mixed convection heat transfer and decrement of drag coefficient in a lid-driven nanofluid-filled cavity with a conductive rotating circular cylinder at different horizontal locations: a sensitivity analysis. *Powder Technol*. 2017;305:495-508.
32. Box GE, Wilson KB. On the experimental attainment of optimum conditions. *J R Stat Soc B*. 1951;13(1):1-38.

How to cite this article: Basir MFM, Bilal M, Choudhary R, Mackolil J, Mahanthesh B, Nisar KS. Numerical and sensitivity analysis of MHD bioconvective slip flow of nanomaterial with binary chemical reaction and Newtonian heating. *Heat Transfer*. 2021;1-28. https://doi.org/10.1002/htj.22132